Microdamage modelling of crack initiation and propagation in FCC single crystals under complex loading conditions

Prajwal A. Sabnis[a], Samuel Forest[a,*], Jonathan Cormier[b]

[a] *Mines ParisTech CNRS Centre des Matériaux UMR 7633, BP 87 91003 Evry, France*
[b] *Institut Pprime, CNRS–ENSMA–Université de Poitiers, UPR CNRS 3346, Département Physique et Mécanique des Matériaux, ISAE–ENSMA–Téléport 2, 1 avenue Cléent Ader, BP 40109, 86961 Futuroscope Chasseneuil Cedex, France*

Abstract

A regularised anisotropic continuum damage mechanics model is presented that couples crystal plasticity with damage induced on crystallographic planes. Two and three-dimensional finite element simulations of crack initiation and propagation in single crystal specimens under complex multiaxial loading with dominating shear are presented for the first time. The crack path in a four-point double notched shear specimen is predicted, in accordance with experimental testing of single crystal nickel-based superalloy AM1. The initiation, bifurcation and propagation of a crack in a shifted double notched specimen under creep conditions is then simulated and compared to the experimental response of nickel-based superalloy MC2 at high temperature. The attention is focused on the influence of coupling between viscoplasticity and damage on the crack path in these single crystals.
© 2016 Elsevier B.V. All rights reserved.

Keywords: Continuum damage mechanics; Micromorphic media; Crystal plasticity; Crack initiation; Crack propagation; Nickel-based superalloy

1. Introduction

The purpose of continuum damage mechanics is to predict the initiation, development and localisation of damage in linear and nonlinear engineering materials [1,2]. In composite materials for instance, a regime of diffuse damage is followed by damage localisation and crack formation leading to final fracture. In quasi-brittle materials or in metals subject to cyclic loading, crack formation and propagation take place rapidly after damage initiation. Initial or induced anisotropy is ubiquitous in damage of materials and represents a challenge for modelling and simulations, as shown by many existing complex formulations of anisotropic damage [3]. In comparison, the applications of continuum damage approaches to metallic single crystals are seldom found in the literature, probably due to the specific anisotropic deformation and damage mechanisms. Creep damage in single crystal nickel-based superalloys was tackled in [4], whereas the authors in [5] proposed a model framework for anisotropic damage coupled to crystal viscoplasticity. Cohesive zone models were used for the simulation of crack propagation along a predefined path in [6] for single

---

ARTICLE IN PRESS

2   *P.A. Sabnis et al. / Comput. Methods Appl. Mech. Engrg. ∎ (∎∎∎∎) ∎∎∎–∎∎∎*

crystal nickel-based superalloys at high temperature. Cohesive zone elements of selected orientation were inserted in [7] to simulate brittle fracture in elastic single crystals.

The influence of crystal plasticity and the role of slip lines for crack initiation in metal single crystals have been extensively documented for monotonic or cyclic loading conditions [8,9]. The formation of intense slip bands or slip localisation promotes crack formation and can dictate the subsequent crack path. Crystal plasticity models were used successfully to simulate the localisation of slip at notches and crack tips and compare with experimental observations of slip activity [10–13]. Damage indicators based on accumulated plastic slip were proposed in [14] and used as a post-processing method to simulate crack propagation in single and polycrystals [15–17]. Crystal viscoplasticity at the crack tip in nickel-based superalloys at high temperature was studied in [18]. It is noticed that, in many cases, the crack follows {111} planes of FCC single crystals which can lead to complex zig-zag paths [17]. This experimental feature was used in [19–21] to elaborate a coupled damage and plasticity continuum model for the simulation of crack initiation and propagation in single crystals.

The simulation of damage localisation by means of the finite element methods is associated with mesh-dependence of computational results. A regularisation procedure based on the micromorphic approach to gradient plasticity and damage was proposed in [19–21]. Micromorphic models involve additional strain-like degrees of freedom and their gradient in the constitutive framework [22]. The micromorphic continuum was used recently for the simulation of quasi–brittle fracture [23] and represents a theoretical and computational alternative to strict gradient damage theory [24]. A single scalar micromorphic variable, called microdamage, is used together with its gradient in the formulation proposed for single crystals in [19,20]. This strategy of a single scalar regularising microdeformation variable was also chosen in [25,26] to model size effects in strain gradient crystal plasticity, the microdeformation variable being akin to the accumulated plastic slip on slip systems.

This continuum gradient damage modelling can be compared to recent phase-field approaches to fracture processes [27–30]. The phase-field order parameter, ϕ, and the classical damage variable, D, live together in the interval [0:1] and similar free energy potential functions of ϕ, $\nabla\phi$, D, ∇D are defined in the respective damage models [31,32]. However continuum damage theory has a longer history for the simulation of crack initiation and propagation so that the corresponding terminology will be used in the following instead of the phase-field one. The phase-field approach has been applied to brittle fracture of elastic single crystals in [33,34]. It was recently combined with crystal viscoplasticity for ductile crystals in [35]. This phase-field model is based on unilateral damaging elasticity and does not introduce the crystallographic damage plane concept of [19,20].

The damage models proposed for single crystals in [19–21] and developed further in the present work differ from classical continuum damage mechanics in so far as the damage variable, d, is a strain–like quantity, therefore unbounded, and not a damage indicator lying in the interval [0:1]. They are therefore closer to Gurson-like ductile fracture models for metals that rely on compressible plasticity modelling. Another significant difference with respect to existing damage model is that the constitutive equations are formulated in such a way that softening occurs as soon as damage initiates. This is in contrast to damage models for composite materials for instance for which a regime of diffuse damage exists prior to localisation. In high strength metallic single crystals, especially nickel-based superalloys, damage has a tendency to localise rapidly after significant amount of plasticity. This is especially the case in fatigue for which the present class of models was developed originally [19,20].

It remains that continuum damage-based simulations of crack propagation in single crystals are very limited in the literature so that significant model development, computational analysis and validation with respect to experimental observations are needed for engineering applications.

The objective of the present work is to test the performance of a regularised continuum damage model for crack initiation and propagation in single crystalline components under complex multiaxial loading and in the presence of strong coupling between crystal viscoplasticity and damage. The proposed microdamage model represents a significant evolution of first formulations presented in [19,20]. It contains two new features making it more easily amenable to 3D computations, namely a reduction of the number of internal variables accompanied with a novel coupling between plasticity and damage to be explicit. The originality of the paper lies in this model formulation and its application to two finite element computations of specimens subjected to complex multiaxial shear dominated loading conditions. The simulation results are compared with experiments performed on single crystal nickel-based superalloys at high temperature. The attention is focused on the influence of coupling between viscoplasticity and damage on the crack path.

ARTICLE IN PRESS

P.A. Sabnis et al. / Comput. Methods Appl. Mech. Engrg. ▊ (▊▊▊▊) ▊▊▊–▊▊▊

3

The micromorphic coupled crystal plasticity and damage model is formulated in Section 2 where the main features of the model are illustrated by first finite element simulations dealing with regularisation properties, plasticity-damage coupling and crack closure effects. A single crystal double notched specimen is considered in Section 3 and subjected to special loading conditions inducing shear and tension–compression in the notched zone. Crack initiation is predicted, followed by crack propagation. Brittle to ductile crack behaviours are illustrated depending on the values of material parameters. The predicted crack paths are compared to the one observed in experiments performed on single crystal nickel-based superalloy AM1 at 950 °C according to [36–38]. Creep loading conditions are investigated in Section 4 where the shear dominated fracture of a single crystal plate with shifted notches is predicted and compared to original experimental results on the single crystal nickel-based superalloy MC2 [39,40].

According to the notation used throughout, first, second and fourth order tensors are denoted by $\underline{a}$, $\underset{\sim}{a}$ and $\underset{\approx}{a}$, respectively. The computational analysis is currently limited to small deformations although the finite deformation formulation of microdamage models for single crystals was presented based on the multiplicative decomposition of the deformation gradient into reversible and irreversible contributions in [21]. The presented physical cases do not involve large strains prior to cracking since damage localises rapidly in nickel-based superalloys. Accordingly large strains will not significantly affect the crack initiation location and first crack path for the shear test considered in Section 3, and the creep test of Section 4.

2. Coupled crystal plasticity and microdamage model

The balance and constitutive equations of the model are presented within the small deformation framework.

2.1. Kinematics and balance equations

The degrees of freedom (DOF) of the microdamage continuum are the displacement vector $\underline{u}$ and an additional strain-like microdamage variable, d_χ. Thus, the set of element DOFs and the extended gradient space are chosen as

$$\text{DOF} = \{\underline{u}, d_\chi\}, \qquad \text{Grad} = \left\{\underset{\sim}{\varepsilon} := \frac{1}{2}(\underline{u} \otimes \nabla + \nabla \otimes \underline{u}), \nabla d_\chi\right\}. \tag{1}$$

The total strain rate tensor is split into three contributions

$$\dot{\underset{\sim}{\varepsilon}} = \dot{\underset{\sim}{\varepsilon}}^e + \dot{\underset{\sim}{\varepsilon}}^p + \dot{\underset{\sim}{\varepsilon}}^d \tag{2}$$

respectively accounting for elastic, crystal plasticity and damage strain mechanisms. As usual in crystal plasticity, the plastic strain tensor $\underset{\sim}{\varepsilon}^p$ is traceless. In contrast, the damage strain is generally not purely deviatoric and includes volume changes induced by microcracking inside the material element. The concept of damage strain was introduced in [19] in the spirit of continuum damage mechanics of ductile fracture. In the context of Gurson-like models, there is no explicit distinction between plastic and damage parts which are all recorded into a generally non deviatoric plastic strain variable and derived from a unified criterion. In the case of single crystals, specific mechanisms will be assigned to plasticity and damage. It is important to insist on the fact that the d_χ variable is not a standard damage indicator with values bounded between 0 and 1, as usual in a broad class of continuum damage models. The microdamage variable d_χ is a strain quantity related to inelastic deformation induced by damage, as will become apparent once the constitutive equations of the model are explicit. This is also in contrast to phase-field variables that are also very often order parameters bounded by 0 and 1.

An enhanced form of the principle of virtual power is considered after [22],

$$\int_{\mathcal{D}} \left(\underset{\sim}{\sigma} : \underset{\sim}{\varepsilon}(\underline{v}^\star) + a \, \dot{d}_\chi^\star + \underline{b} \cdot \nabla \dot{d}_\chi^\star\right) dV = \int_{\partial\mathcal{D}} \left(\underline{t} \cdot \underline{v}^\star + a_c \, \dot{d}_\chi^\star\right) dS \tag{3}$$

for any subdomain $\mathcal{D}$ of the body Ω and any field of virtual velocity $\underline{v}^\star$ and virtual microdamage rate $\dot{d}_\chi^\star$. The generalised stresses a and $\underline{b}$ are introduced in addition to Cauchy's stress tensor, $\underset{\sim}{\sigma}$. The balance equations and associated boundary conditions for the microdamage model are derived from Eq. (3) as,

$$\text{div} \, \underset{\sim}{\sigma} = 0, \qquad \text{div} \, \underline{b} = a \quad \forall \underline{x} \in \Omega \tag{4}$$

ARTICLE IN PRESS

4   *P.A. Sabnis et al. / Comput. Methods Appl. Mech. Engrg.* ∎ *(∎∎∎∎)* ∎∎∎–∎∎∎

$$\underline{\underline{\sigma}} \cdot \underline{n} = \underline{t}, \qquad \underline{b} \cdot \underline{n} = a_c \qquad \forall \underline{x} \in \partial\Omega \tag{5}$$

in the static case and in the absence of body forces [19]. The traction vector is $\underline{t}$ and a_c is a generalised traction.

2.2. Constitutive equations

The free energy density function, Ψ, contains coupled contributions of elasticity, plasticity and damage in the form:

$$\rho\,\Psi(\underline{\underline{\varepsilon}}^e, \gamma, d, d_\chi, \nabla d_\chi) := \rho\,\Psi^e(\underline{\underline{\varepsilon}}^e) + \rho\,\Psi^p(\gamma) + \rho\,\Psi^d(\gamma, d, d_\chi, \nabla d_\chi) \tag{6}$$

where the state variables are defined in the following.

Elastic contribution

The elastic contribution is quadratic with respect to the elastic strain tensor and involves the fourth order tensor of elastic moduli:

$$\rho\,\Psi^e(\underline{\underline{\varepsilon}}^e) = \frac{1}{2}\underline{\underline{\varepsilon}}^e : \underline{\underline{\underline{\underline{C}}}} : \underline{\underline{\varepsilon}}^e. \tag{7}$$

The elasticity moduli could be coupled to damage to describe loss of stiffness induced by microcracking as done in classical continuum damage mechanics, see [41,42] in the case of crystal plasticity and damage. However, this coupling is neglected here. This assumption is made in ductile damage (Gurson potential and models alike) because the plastic deformation dominates the elastic part even in the final stages where the material is severely damaged. This is also the case in the present model coupling crystal plasticity and damage localising rapidly into cracks. This is in contrast to composite materials undergoing more diffuse damage prior to localisation.

Crystal plasticity equations

In Eq. (6), $\rho\,\Psi^p$ represents the plasticity contribution to the free energy in the form of energy storage due to work-hardening, such as non-linear isotropic hardening and kinematic hardening [1]. In the present work, it is assumed to be a function of a cumulative slip variable, γ, considered as a state variable of the model. Because a major portion of the model development presented here was carried out for materials which exhibit an almost linear isotropic hardening plasticity curve, the following simple quadratic form is adopted:

$$\rho\,\Psi^p(\gamma) := r_0\gamma + \frac{h}{2}\gamma^2 \tag{8}$$

where r_0 is the initial threshold and h the linear isotropic hardening modulus. The dependence of the cumulative slip amount γ on slip activity of the N slip systems will be characterised later on. The Eq. (8) corresponds to linear hardening, which is a very simple assumption compared to the actual behaviour of the considered materials. However this choice was made to better control the coupling between plasticity and damage. In particular some analytical solutions could be derived to check the validity of simulations. More sophisticated hardening models can be substituted.

Representation of damage and coupling with plasticity

The function $\rho\,\Psi^d$ in Eq. (6) represents the contributions of damage and the coupling of damage and plasticity to the free energy function. It is assumed to be a function of cumulative slip γ, microdamage d_χ, its gradient, and of a cumulative damage variable, d. The following quadratic form is adopted:

$$\rho\,\Psi^d(\gamma, d, d_\chi, \nabla d_\chi) := Y_0 d + \frac{H}{2}(d + \beta\gamma)^2 + \frac{H_\chi}{2}(d - d_\chi)^2 + \frac{A}{2}\nabla d_\chi \cdot \nabla d_\chi. \tag{9}$$

The regularisation contribution is included in a penalty format, by penalising the difference between the internal variable d and the enhanced degree of freedom d_χ. The model minimises this difference to ensure that the internal variable d and the degree of freedom d_χ remain close. In the development presented here, an isotropic form of the gradient component (∇d_χ) is retained since the work deals with cubic crystals. Coupling between damage and plasticity is achieved through the term $\frac{H}{2}(d + \beta\gamma)^2$. The dependence of the cumulative damage variable d on the damage mechanisms will be characterised later on.

ARTICLE IN PRESS

P.A. Sabnis et al. / Comput. Methods Appl. Mech. Engrg. ▮ (▮▮▮▮) ▮▮▮–▮▮▮

5

State laws and regularisation equation

The thermodynamic forces associated with the state variables $(\underset{\sim}{\varepsilon}^e, \gamma, d, d_\chi, \nabla d_\chi)$ are obtained from partial derivation of the free energy density function, as:

$$\underset{\sim}{\sigma} = \rho \frac{\partial \Psi}{\partial \underset{\sim}{\varepsilon}^e} = \underset{\approx}{C} : \underset{\sim}{\varepsilon}^e \tag{10}$$

$$r := \rho \frac{\partial \Psi}{\partial \gamma} = r_0 + h\gamma + H\beta^2\gamma + H\beta d \tag{11}$$

$$Y := \rho \frac{\partial \Psi}{\partial d} = Y_0 + Hd + H\beta\gamma + H_\chi(d - d_\chi) \tag{12}$$

$$a = \rho \frac{\partial \Psi}{\partial d_\chi} = -H_\chi(d - d_\chi) \tag{13}$$

$$\underline{b} := \rho \frac{\partial \Psi}{\partial \nabla d_\chi} = A\nabla d_\chi \tag{14}$$

where the coupling between plasticity and damage is clearly visible in the material parameter β.

As a consequence of the balance Eq. (4) for the generalised stresses and of the state laws (13) and (14), the microdamage variable is solution of the following partial differential equation:

$$d_\chi - \frac{A}{H_\chi}\Delta d_\chi = d \tag{15}$$

known as a Helmholtz-type regularisation equation and where Δ stands for the Laplace operator [43,22,19]. This equation involves the characteristic length

$$\ell_c = \sqrt{\frac{A}{H_\chi}}. \tag{16}$$

Other characteristic length scales can be defined in the model by combining plastic moduli and the higher order modulus A, see [19]. The thermodynamic force a appears in the balance Eq. (4)$_2$. When the constitutive Eqs. (13) and (14) are substituted into this balance equation, the regularisation operator (15) is obtained.

Yield and damage criteria; Dissipation potential

The plastic yield criterion considered here corresponds to the classical *Schmid* law in crystal plasticity theory. The driving forces for slip system activation are the resolved shear stresses, τ^s, on the N slip systems.

$$f_p^s = |\tau^s| - r, \quad \text{with } \tau^s = \underline{n}^s \cdot \underset{\sim}{\sigma} \cdot \underline{\ell}^s \tag{17}$$

where $\underline{n}^s$ is the normal to the slip plane of slip system s and $\underline{\ell}^s$ is the corresponding slip direction. There are therefore N such yield criteria. The list of slip systems considered in this work are given in Table 3. There are 4 slip planes {111} and 3 slip directions ⟨110⟩ contained in these planes, which leads to 12 slip systems. They correspond to the $N = 12$ slip systems of FCC crystals. The critical resolved shear stress is the variable r, defined by the Eq. (11).

The driving force for damage is assumed to be the normal stress component on each of the previous slip planes. In FCC crystals, there are four such slip planes which leads to the definition of four damage criteria:

$$f_d^r = |\sigma_n^r| - Y, \quad \text{with } \sigma_n^r = \underline{n}^r \cdot \underset{\sim}{\sigma} \cdot \underline{n}^r \tag{18}$$

where the label $r \in \{1, \ldots, N^d\}$. The damage planes coincide with the 4 slip planes {111}: $N^d = 4$. The labelling of these damage planes is given in Table 3. Each criterion f_d^r is reminiscent of a cleavage condition, well-known in brittle crystals [44,45], except that only positive σ_n can cause cleavage, whereas its absolute value is considered here for reasons explained in Section 2.4.

The presented constitutive model differs from the ones used in [19,20]. It brings two new features making it more easily amenable to 3D computations. It contains first a simplification which is regarded as a true improvement of the

ARTICLE IN PRESS

6   *P.A. Sabnis et al. / Comput. Methods Appl. Mech. Engrg. ▮(▮▮▮▮) ▮▮▮–▮▮▮*

model. In [19,20], three internal variables were attributed to each crystallographic damage plane corresponding to cleavage crack opening (mode I damage type) and in-plane shear accommodation (mode II and III damage modes), respectively. The shear damage accommodation variables have been suppressed in the present version of the model, thus sparing 8 (twice the number of damage planes) variables to be numerically integrated. In the new model, the mode II and III damage components are accommodated by the plastic slip variables themselves, once cleavage opening is started. Once cleavage-like damage occurs, the critical resolved shear stress decreases (softening) so that mode II and III damage modes can be accommodated by the slip variables, as will be illustrated in Section 2.4. This is made possible by a second new feature of the model, namely the coupling between the damage variable d and the cumulated plastic slip γ in Eqs. (11) and (12). The free energy potential (9) involving the damage variable is different from the one used in [20,21] where the mixed term γd is absent.

It is also noted that the critical resolved shear stress r is the same for all slip systems even in the presence of hardening. Similarly, the critical normal stress Y is the same for all fracture planes. This is a simplification which turns out to be sufficient for the nickel-based superalloys at the considered temperatures. In particular, there is no interaction matrix between slip systems as identified in [46].

The dissipation rate per unit volume is defined as usual as [47]:

$$D = \underset{\sim}{\sigma} : \dot{\underset{\sim}{\varepsilon}} - \rho \dot{\Psi} \geq 0. \tag{19}$$

Taking the state laws into account leads to the following form of the residual dissipation:

$$D = \underset{\sim}{\sigma} : \dot{\underset{\sim}{\varepsilon}}^p + \underset{\sim}{\sigma} : \dot{\underset{\sim}{\varepsilon}}^d - R\dot{\gamma} - Y\dot{d} \geq 0. \tag{20}$$

The dissipation is therefore due to the inelastic power diminished by the energy stored by hardening and damage.

The evolution equations for plastic and damage strain are deduced from a viscoplastic dissipation potential function of the stress tensor and of the thermodynamic forces r and Y:

$$\Omega(\underset{\sim}{\sigma}, r, Y) := \sum_{s=1}^{N} \frac{K}{n+1} \left\langle \frac{f_p^s(\underset{\sim}{\sigma}, r)}{K} \right\rangle^{n+1} + \sum_{r=1}^{N^d} \frac{K_d}{n_d+1} \left\langle \frac{f_d^r(\underset{\sim}{\sigma}, Y)}{K_d} \right\rangle^{n_d+1} \tag{21}$$

which corresponds to power law models with exponents n, n_d and viscosity parameters K, K_d. The inelastic strain rate is derived as

$$\dot{\underset{\sim}{\varepsilon}}^p + \dot{\underset{\sim}{\varepsilon}}^d = \frac{\partial \Omega}{\partial \underset{\sim}{\sigma}} \tag{22}$$

and the plastic and damage strain rates are identified as:

$$\dot{\underset{\sim}{\varepsilon}}^p := \sum_{s=1}^{N} \dot{\gamma}^s \, \underline{n}^s \otimes \underline{\ell}^s \, \text{sign} \, \tau^s, \quad \text{with } \dot{\gamma}^s = \left\langle \frac{f_p^s}{K} \right\rangle^n \tag{23}$$

$$\dot{\underset{\sim}{\varepsilon}}^d := \sum_{r=1}^{N^d} \dot{d}^r \, \underline{n}^r \otimes \underline{n}^r \, \text{sign} \, \sigma_n^r, \quad \text{with } \dot{d}^r = \left\langle \frac{f_d^r}{K_d} \right\rangle^{n_d}. \tag{24}$$

The amount of slip for each slip system is γ^s whereas d^r denotes the damage strain induced by the damage plane r, represented by the opening of microcracks perpendicular to the fracture plane r.

From Eqs. (23) to (24), it can be seen that the plastic strain is purely deviatoric and that the damage strain contains a spherical part. So, volume changes can be attributed to the damage strain solely. In contrast, it is not possible to distinguish the deviatoric parts related to plasticity and damage. This is a new feature of the model, namely that the shear related damage is accommodated by both plasticity and damage flow rules.

Finally, the evolution laws for the internal variables γ and d are also derived from the viscoplastic potential as:

$$\dot{\gamma} = -\frac{\partial \Omega}{\partial r} = \sum_{s=1}^{N} \dot{\gamma}_s, \qquad \dot{d} = -\frac{\partial \Omega}{\partial Y} = \sum_{r=1}^{N^d} \dot{d}^r. \tag{25}$$

These variables represent the cumulative slip and damage, respectively.

ARTICLE IN PRESS

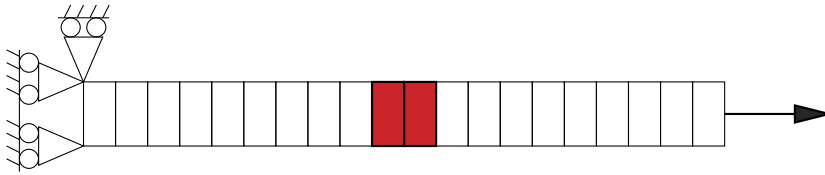*P.A. Sabnis et al. / Comput. Methods Appl. Mech. Engrg. ▮ (▮▮▮▮) ▮▮▮–▮▮▮* 7

Fig. 1. Tensile test on a material bar. The red elements have been artificially weakened to trigger damage localisation. The length of the bar is 10 mm. (For interpretation of the references to colour in this figure legend, the reader is referred to the web version of this article.)

The convexity of the viscoplastic potential Ω with respect to its arguments then ensures the positivity of the residual dissipation [1].

The present model is such that the generalised stresses $\underline{b}$ and a are non dissipative and directly characterised by the state laws (13) and (14). As a result, they do not arise in the dissipative potential (21). The field d_χ is solution of the static Eq. (15) which does not contain any time derivative of d_χ. This is in contrast to phase-field models which introduce such a dissipative part and for which the time derivative of the phase-field arises in the Landau–Ginzburg balance/evolution equation, see [48].

2.3. Finite element implementation

The model was implemented in the implicit finite element code Zset [49]. Finite elements with quadratic interpolation for displacement and microdamage, and reduced integration are used in all the meshes presented in this work. Each node is endowed with 4 degrees of freedom, namely the displacement components U_i, $i \in \{1, 2, 3\}$ and the microdamage variable, d_χ. A variant consists in using quadratic interpolation for the displacement components and linear interpolation for the microdamage degrees of freedom. It was tried in [20] with a similar model, without real benefit, due to the fact that most of the CPU time is spent in the numerical integration of the constitutive equations in the crack process zone. Note also that the authors in [50] use linear conformal elements for isotropic strain gradient plasticity applied to ductile fracture.

A Newton–Raphson algorithm is used for the global resolution of static equilibrium [1]. The weak formulations of the problem and the associated matrix formulation for finite elements can be found in [20].

A fourth order Runge–Kutta method with automatic time-stepping is used for the integration of the differential equations for the internal variables of the model. An alternative is to resort to an implicit θ–method for the integration. The corresponding consistent tangent matrices were derived for the earlier version of the proposed model in [20].

2.4. Application to a bar under tension

To exhibit the basic features of the model, the present section provides some numerical tests carried out on a simple bar under monotonic tension until fracture. An imperfection is introduced in the centre of the bar to trigger damage localisation, as shown in Fig. 1. Fig. 2 summarises the characteristic response of the model. As the loading is imposed, one observes the linear evolution of the von Mises stress into the elastic regime and then into the plastic regime with plastic modulus $h + H\beta^2$ defined in Eq. (11) (red curve in Fig. 2). The blue and green curves respectively show the evolution of the critical resolved shear stress and damage threshold. The former increases linearly as soon as the yield stress is reached, whereas the latter decreases (negative damage modulus βH in Eq. (12)). At the intersection of the stress and damage stress threshold curves, damage initiation occurs in the material. This corresponds also to an abrupt change in the decreasing slope of the variable Y (negative modulus H in Eq. (12)). It is a specific feature of the model: damage localises as soon as it occurs, after a relatively long plastic regime. This corresponds to the physical reality, for instance in single crystal nickel-based superalloys, especially in fatigue, that damage zones are very limited spatially [20]. Furthermore, it is also seen that the plastic threshold begins to decrease simultaneously, due to the coupling between plasticity and damage (negative modulus H in Eq. (11)). Finally, once the damage threshold reaches zero, the material is considered as broken and does not offer any resistance to further inelastic deformation. This is implemented by the artificial and abrupt change of the plastic threshold to zero. Note that the final stress value in the broken element in Fig. 2 is not exactly zero, but a small non-vanishing value associated with the residual viscous stress contribution associated with parameters K, K_d, n, n_d.
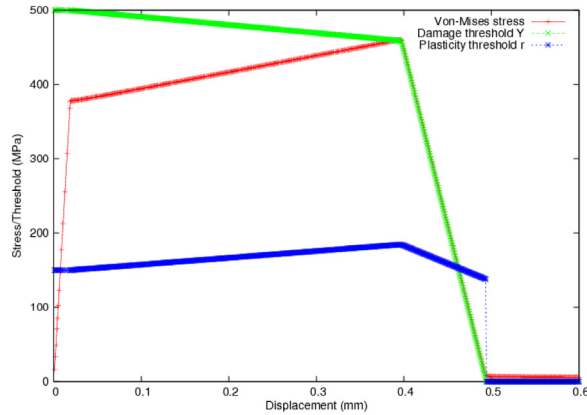
ARTICLE IN PRESS

8   *P.A. Sabnis et al. / Comput. Methods Appl. Mech. Engrg. ▮ (▮▮▮▮) ▮▮▮–▮▮▮*

Fig. 2. Evolution of stress σ, damage threshold Y, plastic threshold r w.r.t. to the applied displacement during the tensile test of Fig. 1. A single damage plane perpendicular to the load is used for this example. The material parameters are $r_0 = 150$ MPa, $Y_0 = 500$ MPa, $h = 100$ MPa, $H = -5000$ MPa, $\beta = 0.1$. (For interpretation of the references to colour in this figure legend, the reader is referred to the web version of this article.)
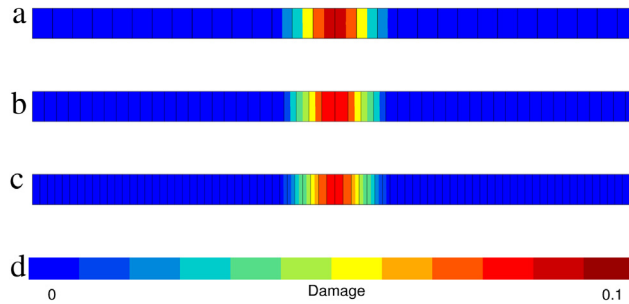
Fig. 3. Regularised damage in a bar in tension. Distribution of damage strain at a given load in the softening regime for three different mesh sizes.

The multi-linear evolution of plasticity and damage threshold functions represent simplifications of the actual material response. Non-linear hardening or softening laws can be introduced but make the analysis of the properties of the proposed model harder to control. That is why the present paper concentrates on such simplified laws.

The microdamage model introduces a constitutive parameter $A > 0$ to control the width over which damage is regularised. Fig. 3 shows the bar example with different finite element discretisations. By keeping the parameter A and specimen size constant, and decreasing the element size, it is seen that the damage zone width remains unchanged, as expected and as analysed in more detail in [19] using a similar regularisation strategy. In the broken state, the higher order modulus A is set to a very small ultimate value since the element cannot store any energy any more.

The microdamage model also makes use of the coupling modulus H_χ which acts as a penalty factor in the free energy function (9) ensuring that the microdamage variable d_χ remains close to the cumulative damage variable d. This implies that the regularised microdamage zone, solution of the partial differential equation (15) coincides with the localised damage zone. This can be checked by plotting the values of d and d_χ against plastic strain, as done in Fig. 4.

2.5. Multi-modal damage and crack closure effects

In the presented model, a point to be noted is that the accumulated damage only contains a contribution from "opening" mechanisms on the damage planes, corresponding to mode I loading with respect to these planes, represented by the normal opening mode $\underline{n}^r \otimes \underline{n}^r$ in Eq. (24). This raises a question regarding the effects of shear type loading modes II and III with respect to the damage planes. In the model proposed in [19,20], specific shear damage modes were introduced for that purpose in the form of so-called accommodation damage systems associated with two additional internal variables for each damage planes. As a model simplification, this is not the case in the present
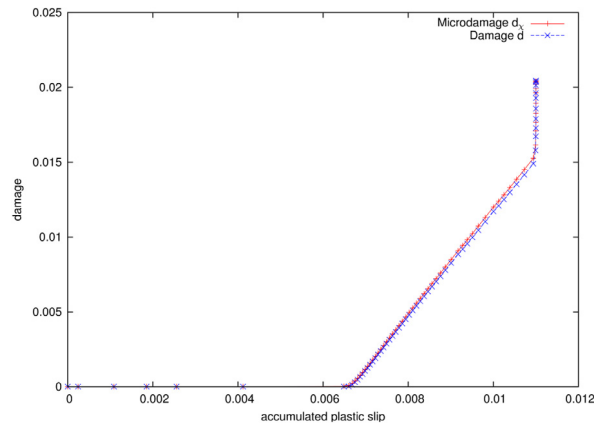
ARTICLE IN PRESS

P.A. Sabnis et al. / Comput. Methods Appl. Mech. Engrg. ▮ (▮▮▮▮) ▮▮▮–▮▮▮   9

Fig. 4. Evolution of damage strain d and microdamage d_χ w.r.t. the evolution of accumulated plastic slip. The damage and the microdamage variables are almost coincident, thereby indicating the constraint induced by the high value of material parameter H_χ. The values used for the simulation are $A = 33\,333$ MPa mm^2, $H = -26\,000$ MPa, $H_\chi = 100\,000$ MPa.

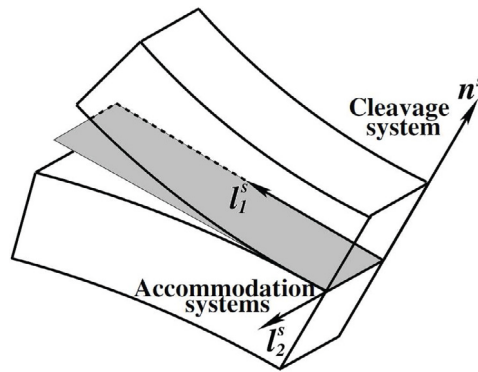Fig. 5. Simple representation of concepts of opening and accommodation slip systems: the normal to the damage/cleavage plane is $\underline{\boldsymbol{n}}^s$ and $\underline{\boldsymbol{\ell}}_1^s$ and $\underline{\boldsymbol{\ell}}_2^s$ represent the accommodation directions.

formulation. The simplification is valid for FCC crystals for which the damage planes coincide with the slip planes (see Table 3). In that case, the accommodation damage systems defined in [19,20] coincide with the slip systems. In the present model, the physical assumption is that a mode I loading component on one damage plane is necessary to reach the threshold Y and trigger damage. Once damage starts, rapid softening occurs both for the damage and plasticity thresholds due to the coupling β. As a result, plasticity will accommodate the mode II and III loading components in each damage plane. Note that in most loading conditions encountered in specimens and industrial components, a non–vanishing normal stress component on one damage plane at least exists and is a prerequisite for damage to occur. A schematic representation of this concept of opening plane and accommodation systems lying in the damage plane is illustrated in Fig. 5. This mechanism is illustrated in the next example dealing with crack closure effects and in Section 3 dedicated to a shear specimen combining all modes due to the complex stress fields.

The treatment of crack closure is an essential issue in continuum damage mechanics [1] where conditions of unilateral contact between crack surfaces must be reflected in the continuum setting. Such conditions are especially difficult to describe in the context of initially isotropic materials where the crack surface is geometrically unknown [3,51]. In contrast, in the case of single crystals, the condition of crack opening and closure can be tested with respect to the chosen crystallographic crack plane mechanisms even though the actual crack path is not necessarily crystallographic due to the superposition of the damage mechanisms. This question is particularly acute in the case of cyclic loading addressed in [19] but it arises also in the context of multiaxial loading where closing can take place in the damage process zone even though the formed crack remains open, for instance after crack bifurcation or branching. The present model is extended in this section to address unilateral effects but does not examine the question of friction
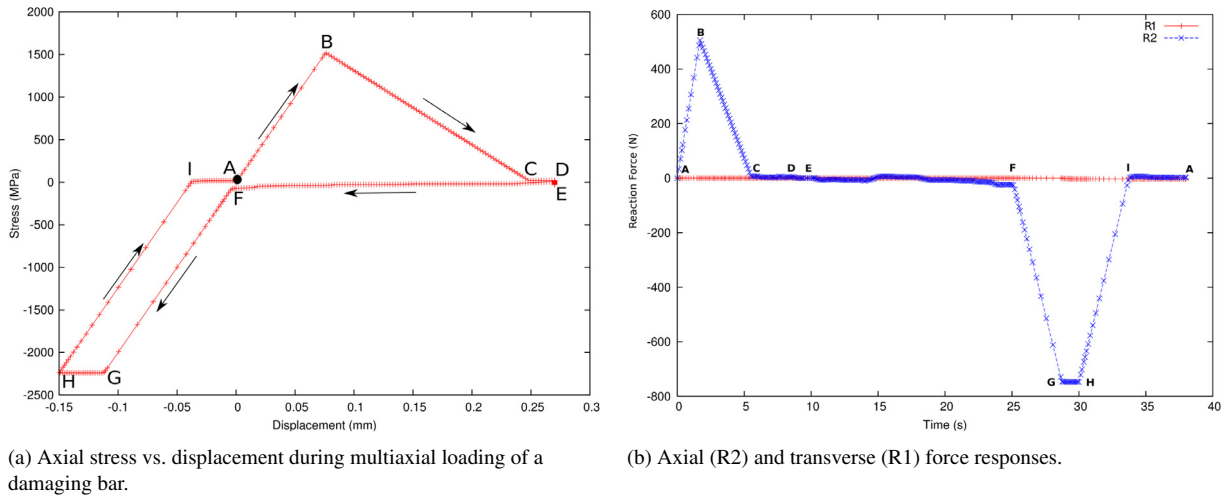
ARTICLE IN PRESS

10   P.A. Sabnis et al. / Comput. Methods Appl. Mech. Engrg. ▮ (▮▮▮▮) ▮▮▮–▮▮▮

(a) Axial stress vs. displacement during multiaxial loading of a damaging bar.

(b) Axial (R2) and transverse (R1) force responses.

Fig. 6. Multiaxial loading of a damaging bar: stress vs. displacement responses.

in the damage zone which represents a future subtle issue. In the present model, the microcrack is said to be open as soon as one opening mode $d^r > 0$. The case of $d^r \leq 0$ indicates closure of the crack. In the case of $d^r \leq 0$ and $\text{sign}(\sigma_n) < 0$, the condition $\dot{d}^r = 0$ is enforced to prevent further penetration. In other cases, evolution of damage is possible, provided that the yield condition $f_d^r > 0$.

To illustrate the implementation of the crack closure mechanism, one cycle of displacement controlled loading was imposed on the bar of Fig. 1. A single opening plane perpendicular to the tensile axis is chosen in this example. The uniaxial loading was imposed up to complete failure of the material in the tensile part of the loading curve (section ABCD in the figure), and to complete closure of the crack in the compressive part of the loading cycle, after unloading (section DEF in the figure). The axial stress/displacement sequence is shown in Fig. 6(a). During unloading and before crack closure, relative lateral displacements between top and bottom faces were imposed to the specimen to check that the structure does not offer any resistance to shear forces, as shown in Fig. 6(b) plotting the axial and shear stresses. Once the opening variables d^r reach 0 representing crack closure, an elastic response of the material is retrieved (section FG in the figure). The compression was continued so as to enter elastic–plastic regime of the material response, as seen in Fig. 6(a) (section GH). Subsequent unloading to zero stress shows that the bar is still broken into two parts (section IA). For this illustrative simulation, the initial critical resolved shear stress r_0 was chosen higher than the damage threshold Y_0 to obtain brittle fracture in tension. The yield stress was overcome only in compression at higher stresses.

This treatment of crack closure is a specific feature of the proposed model. In Eq. (24), each d^r variable represents the opening strain perpendicular to the cleavage plane r. The corresponding cleavage microcrack is closed when $d^r = 0$. The normal stress to each plane r does not control the closing of the crack, in contrast to several existing unilateral damage models. In Fig. 6(a) representing the opening and closing of a smeared out cleavage crack, it can be seen that the normal stress is small but negative during the closing of the crack. This is due to the fact that the damage model is treated like a plasticity model with a small but non-zero yield value for activation of damage. The proposed continuum model mimics the opening and closing of a crack smeared out over the material element.

3. Simulation of cracking under shear loading conditions

The objective of this section is to apply the proposed theory and computational method to remarkable experiments of four-point loading of a single crystal double notched bar. These experiments were performed within the European project described in [36]. The loading results in dominant shearing of the material. The shear testing of single crystal nickel-based superalloys and its analysis by means of finite element simulations go back to the pioneering works [52,53] in the case of creep loading. The following simulations are performed under monotonic loading for the single crystal nickel-based superalloy AM1 at 950 °C. The simulation results will be compared to the experimental ones

ARTICLE IN PRESS

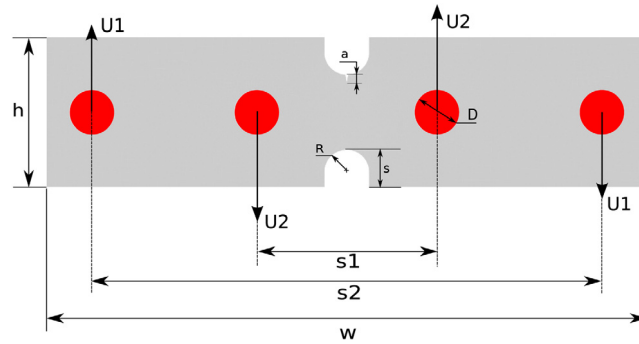*P.A. Sabnis et al. / Comput. Methods Appl. Mech. Engrg.* ▮ *(▮▮▮▮)* ▮▮▮–▮▮▮ 11

Fig. 7. Geometry of the specimen used for testing crack propagation under Mode II loading.

Table 1
Dimensions of the specimen for Mode II test, see Fig. 7.

Dimension	Value (in mm)
Width 'w'	80.0
Height 'h'	20.0
Notch radius 'R'	3.0
Notch height 's'	5.0
Pre-crack length 'a'	1.15
Diameter of holder 'D'	6.0
Distance between inner holders '$s1$'	24.0
Distance between outer holders '$s2$'	68.0

from [36,54] regarding location of crack initiation and crack paths. The comparison remains however qualitative since the experimental loading was low cycle fatigue in contrast to the monotonic simulation.

3.1. Experimental setup and specimen geometry

The considered experiment was carried out at IMMG (Athens, Greece), as part of the SOCRAX project, whose principal objective was the study of propagation of short cracks in single crystal nickel-based superalloys specimens. The experimental setup and the electrical method for detection of crack propagation are described in Refs. [37,38].

The specimen used for the study is shown in Fig. 7. It is a rectangular bar with two opposite notches of radius R. The details of the geometric dimensions of the specimen are given in Table 1. The red regions show the rigid holders used to impose displacement controlled loading $U2, U1$ on the specimen, with $U2 > U1$. A finite element study of the stresses in the specimen reported in [54], showed that shear stresses were dominant in the region between the two notches. It follows that the crack growth observed in this region is driven primarily by in-plane shear and hence, represents a Mode II propagation of cracks in single crystals [36]. Two-dimensional simulations are considered for this mode II test under plane strain conditions due to the fact that in-plane shear is dominating in the deformation zone of the specimen, even though more precise description of the test requires 3D simulations.

The mesh used for the present simulations is shown in Figs. 8(a) and 8(b). The average size of the elements in the central zone (zone of stress concentration) is around 100 μm, and the elements near the tip of the pre-crack are around 20 μm in size. Loading was imposed in the vertical direction, which was aligned with the [001] direction of the crystal. The horizontal axis was aligned along the [010] direction. The small crystal misorientations with respect to the specimen length/width/thickness observed in the experiment are neglected in the simulation.

In the experimental specimens, a pre-crack of length a was introduced to localise crack initiation. In the computation, a sharp V-notch of the same length was introduced instead, to avoid contact of crack lips during testing, see Fig. 8(b).

The material parameters used for the simulation corresponding to AM1 at 950°C are presented in Table 4 in the Appendix. Cubic elasticity and linear plastic hardening before damage starts are used. The additional parameters

ARTICLE IN PRESS

12   *P.A. Sabnis et al. / Comput. Methods Appl. Mech. Engrg.* ▮ *(▮▮▮▮) ▮▮▮–▮▮▮*
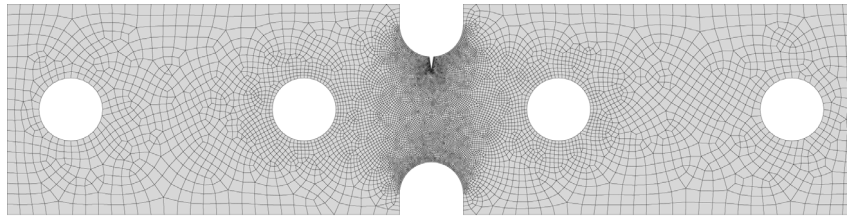
(a) Mesh for complete specimen.
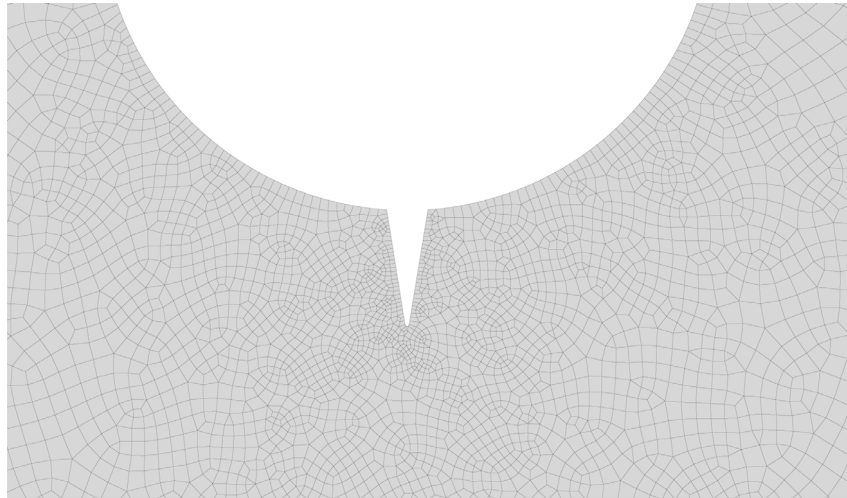
(b) Close-up view of mesh around notch.

Fig. 8. Mesh used in the simulation of Mode II crack propagation (Holders not shown).

introduced in the microdamage model for damage and regularisation are varied in the next section in a parametric study.

3.2. Simulation results and parametric study

The displacements $U1$ and $U2$ of Fig. 7 are imposed proportionally, up to the maximal values $|U2| = 2.83$ mm and $|U1| = 1$ mm. The sample undergoes first elastoviscoplastic deformation until a crack starts from the V-notch and propagates through the sample accompanied by further elastoviscoplastic straining of some parts of the sample. The regularising parameters are fixed to the values $A = 50$ MPa mm^2 and $H_\chi = 100\,000$ MPa providing the characteristic length $\ell_c = 22$ μm according to Eq. (16). This value sets a minimal resolution for crack thickness, see [19,20]. The value of the penalty parameter H_χ is high enough to ensure that the micromorphic model response is close to that of the associated gradient damage model. The initial cleavage stress is set to the value $Y_0 = 1500$ MPa and the material parameter to be varied is the softening modulus H in Eqs. (11) and (12), the plasticity-damage coupling parameter being fixed to the value $\beta = 0.35$.

The influence of the softening parameter H on the crack path is illustrated in Fig. 9. Damage is strongly localised and no diffuse damage zone is observed. Low absolute values of softening favour the formation of a shear band becoming a vertical crack in Fig. 9(a) and (b). Some branching is also observed in this regime. Larger values induce a deviation of the crack to the right in Fig. 9(c), fracture being then more driven by normal stresses than by shear plasticity. The deviation of the crack can be explained by the dominant shear stress in the zone between the U-notch and the inclined {111} damage planes due to the orientation of the sample.

The crack growth history is shown in Fig. 10 where the initiation, propagation and final deviation of the crack are observed. The contour maps of the von Mises stress confirm that the simulated localised damage zones are actual cracks with the expected stress concentration at the moving crack tip. In the fifth comparison stages, two separate stress
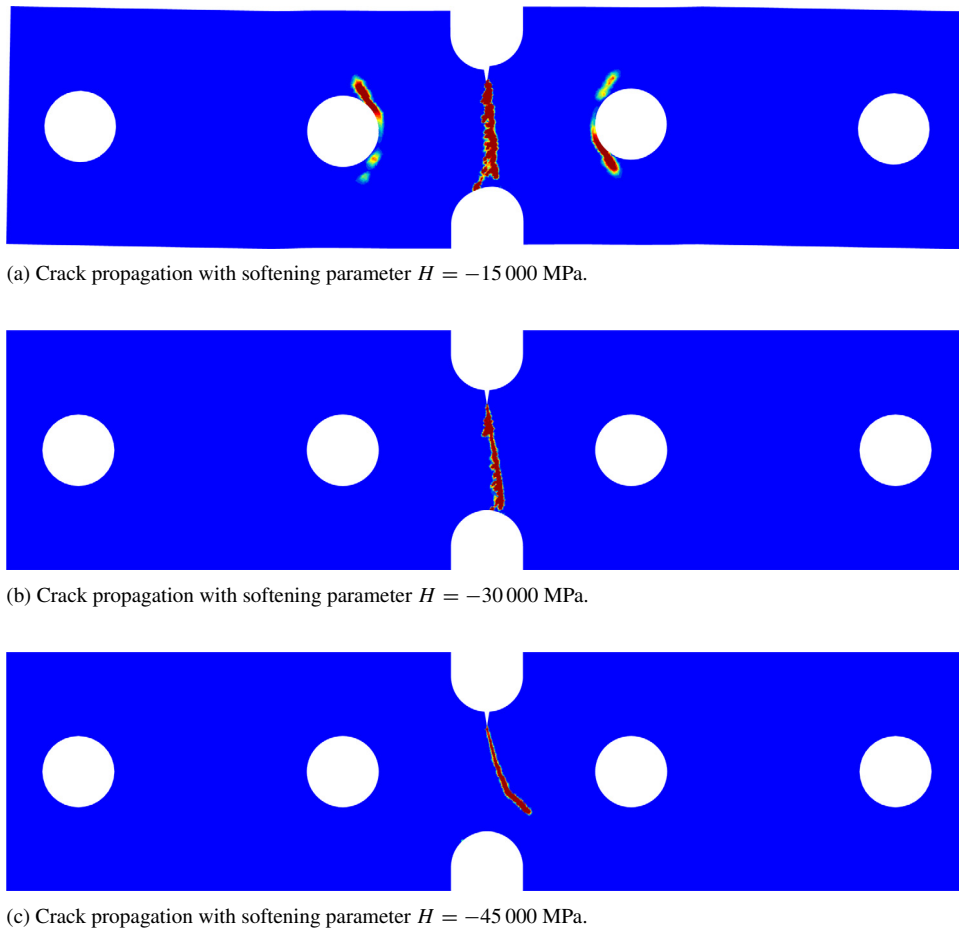
ARTICLE IN PRESS

P.A. Sabnis et al. / Comput. Methods Appl. Mech. Engrg. ▮ (▮▮▮▮) ▮▮▮–▮▮▮　　　　　13

(a) Crack propagation with softening parameter $H = -15\,000$ MPa.

(b) Crack propagation with softening parameter $H = -30\,000$ MPa.

(c) Crack propagation with softening parameter $H = -45\,000$ MPa.

Fig. 9. Effect of softening modulus H on the crack path in the mode II test.

concentration zones are seen, indicating the beginning of branching of the main crack. In the last map, the initiation of smaller cracks is observed at the lower U-notch of the specimen. One of these newer cracks, which is located closer to the existing longer crack, becomes the dominant crack and propagates, while the newly initiated cracks further away from the longer crack do not propagate. Finally, this younger propagating crack joins the second branch of the older crack, and the first branch of the old crack also bifurcates to join the younger crack, thereby resulting in complete material failure. These observations highlight the capability of the microdamage model to handle the initiation and propagation of multiple cracks, in addition to the capability of handling complex cracking phenomena such as branching and bifurcation. However a quantitative analysis of these phenomena would require a finite element analysis at finite strains.

The simulations illustrate the competition in the model between plasticity-driven and normal-stress driven damage, the latter being promoted by high values of $|H|$ and leading to crystallographic cracks parallel to one {111} plane or a combination of these. Lower values also promote multiple successive microbranching of the main crack along the main path, as can be seen from Fig. 9(a, b, c).

3.3. Comparison with experimental results

Fig. 11(a) and (b) show experimental observations of short crack propagation in the actual tests performed at IMMG (two different samples). The observed free surfaces are blurred because of oxidation taking place at 950 °C in spite of the low air pressure of 1 kPa during the test. The tests were performed under force control and the shear stress, defined as the force divided by the lowest section, was cycled between 150 MPa and 250 MPa leading to
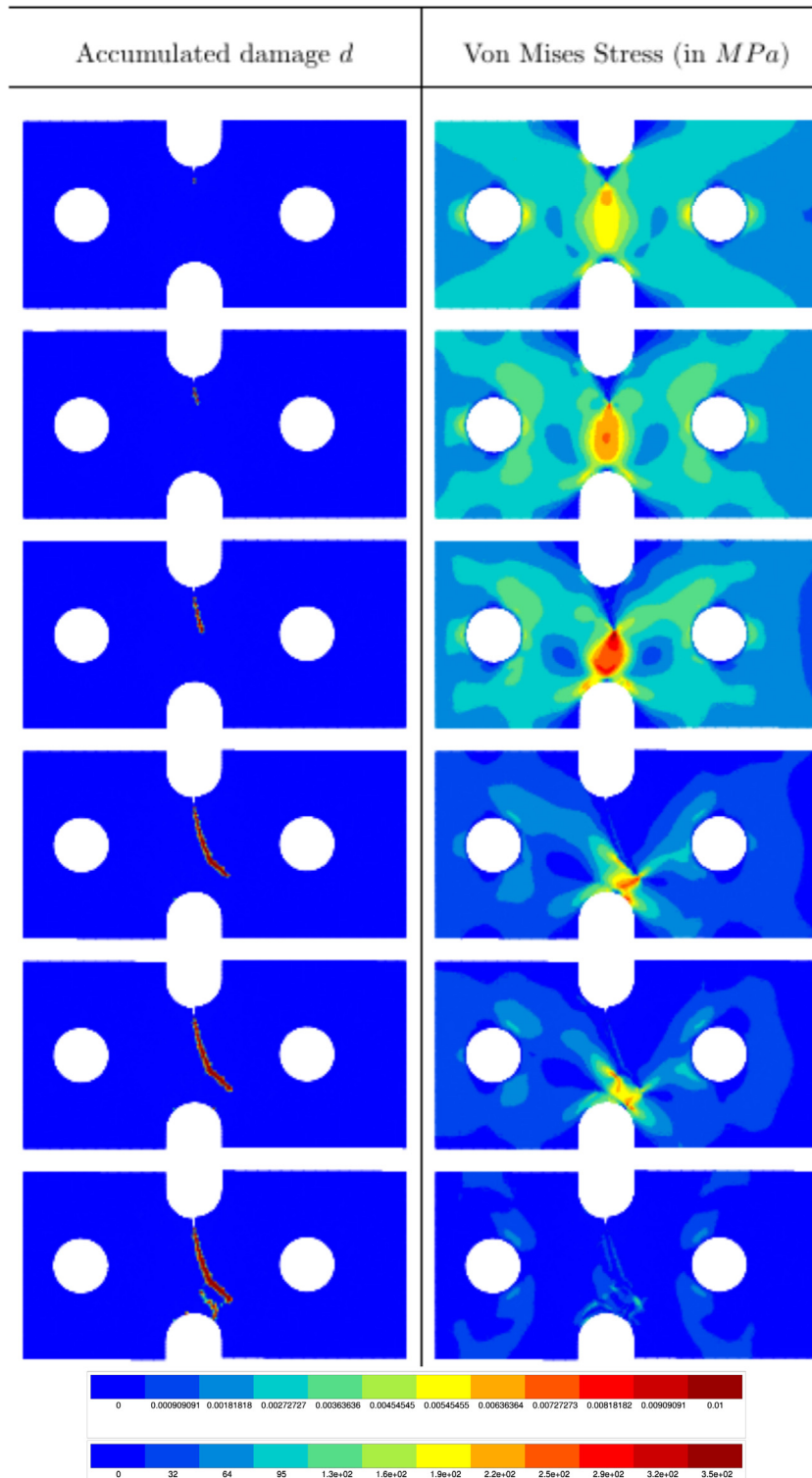
ARTICLE IN PRESS

14 *P.A. Sabnis et al. / Comput. Methods Appl. Mech. Engrg. ▮ (▮▮▮▮) ▮▮▮–▮▮▮*

Fig. 10. Different stages of crack propagation in the Mode II test specimen for $H = -45\,000$ MPa: damage strain d field (left column) and von Mises stress field (right column). The colour scales for damage (top) and stress (bottom) are given below. (For interpretation of the references to colour in this figure legend, the reader is referred to the web version of this article.)
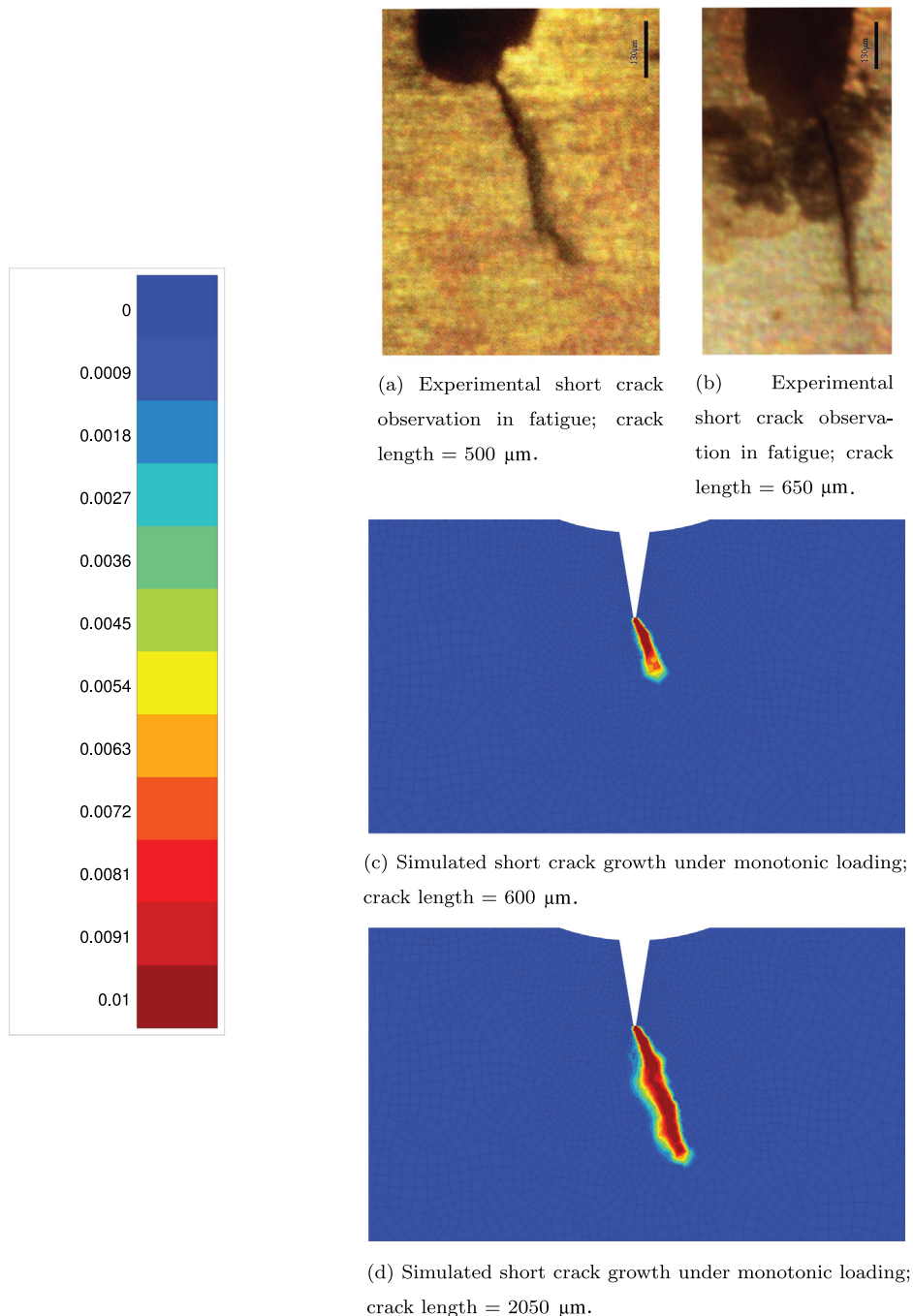
ARTICLE IN PRESS

P.A. Sabnis et al. / Comput. Methods Appl. Mech. Engrg. ▮ (▮▮▮▮) ▮▮▮–▮▮▮ 15

(a) Experimental short crack observation in fatigue; crack length = 500 μm.

(b) Experimental short crack observation in fatigue; crack length = 650 μm.

(c) Simulated short crack growth under monotonic loading; crack length = 600 μm.

(d) Simulated short crack growth under monotonic loading; crack length = 2050 μm.

Fig. 11. Results from Mode II crack growth tests; Simulated crack paths are presented in the form of contour plots of the accumulated damage variable d. Figures (a) and (b) are taken from [36].

progressive deformation and cracking starting from the initial precrack. The fact that significant ratcheting occurs at such asymmetric loading makes reasonable the comparison with the monotonic simulations considered earlier, at least qualitatively. The contour plots of crack path development (contour map of accumulated damage variable, d) of Fig. 11(c) and (d) show crack paths similar to the experimental ones which correspond to a deviation of the crack away from the smallest section of the bar. The observed crack path can be used to identify the suited softening modulus H, as done here with $H = -40\,000$ MPa.

ARTICLE IN PRESS

16 *P.A. Sabnis et al. / Comput. Methods Appl. Mech. Engrg. ∎ (∎∎∎∎) ∎∎∎–∎∎∎*

Table 2
Dimensions of specimen for the creep test.

Dimension	Value (in mm)
Width 'w'	4.0
Height 'h'	24.0
Fillet Radius 'R'	0.9
Notch height 's'	1.0

4. Simulation of cracking under multiaxial creep loading conditions

Creep is a fairly common occurrence in single and polycrystalline alloys, especially in high temperature uncooled components such as the ones used in aircraft and helicopter engines. Sustained loads at extremely high temperatures, combined with processes such as oxidation cause the superalloys to deform and tear at loads well below the ultimate strength of the material. Thus, creep phenomena in single crystal nickel-based superalloys are a point of focus in many studies, see for example [55–59].

The second boundary value problem considered in this work is again dedicated to shear-dominated plasticity and damage, but in the case of creep deformation at very high temperature. Creep simulations are performed in 2D and 3D. A comparison with experimental results is also provided.

4.1. Experimental setup and specimen geometry

Among the many creep experiments available in literature [60–62] etc., the experiment reported in [63] was selected for the simulation because its interpretation requires finite element simulations due to the non-homogeneous deformation induced by the complex geometry. The asymmetric specimen is shown in Fig. 12 and the geometrical dimensions are given in Table 2. It has been designed so as to induce a significant shear component in the stress concentration zone induced by the two shifted notches, in addition to axial loading. The corresponding two-dimensional finite element mesh is also shown in Fig. 12, together with a zoom at the notched region.

The considered material is the single crystal nickel-based superalloy MC2, closely related to AM1 and with similar mechanical properties. The test was performed at the very high temperature of 1050 °C. Experiments under various environmental conditions have shown that crack initiation and first stages of propagation are not oxidation driven. The specimen was loaded up to a $440N$ force which was then maintained constant. The macroscopic load is along a [001] orientation (3°–4° of primary misorientation, neglected in the simulation) while the flat surfaces of the samples are close to (100) planes. The simulation reproduces the exact geometry and loading conditions.

The material parameters of the underlying classical crystal plasticity model, were identified from uniaxial tension and creep tests [60]. They are given in Table 4. The finite element simulation of Fig. 13 is based solely on crystal plasticity modelling and does not include the damage part of the model. It shows that the viscoplastic strain localises between the stress concentrators, as expected. The overall strain[1]–time curve of Fig. 14(a) shows that the model predicts primary and secondary/steady state creep behaviours in reasonable agreement with the beginning of the experimental curve. In contrast, the experimental creep curve also exhibits a tertiary creep domain associated with crack initiation and propagation to be simulated in the next section using the microdamage model. Since damage initiation at this temperature is plasticity driven, the initiation and growth of a crack are expected to occur in the deformed zone of Fig. 13.

4.2. Creep simulation results and comparison with experimental observations

The identification of damage parameters is performed by calibration with respect to the overall creep curve of Fig. 14. These parameters include H_χ, A, H and β. The penalty factor is again chosen high enough for microdamage and damage variables, d and d_χ, to be practically identical, here $H_\chi = 50\,000$ MPa. The higher order modulus is fixed to $A = 0.5$ MPa mm^2. This implies a characteristic length $\ell_c = 3$ µm, setting the resolution of the simulation. This

---

[1] The overall strain is computed based on two selected points not too close to the notched zone.

ARTICLE IN PRESS

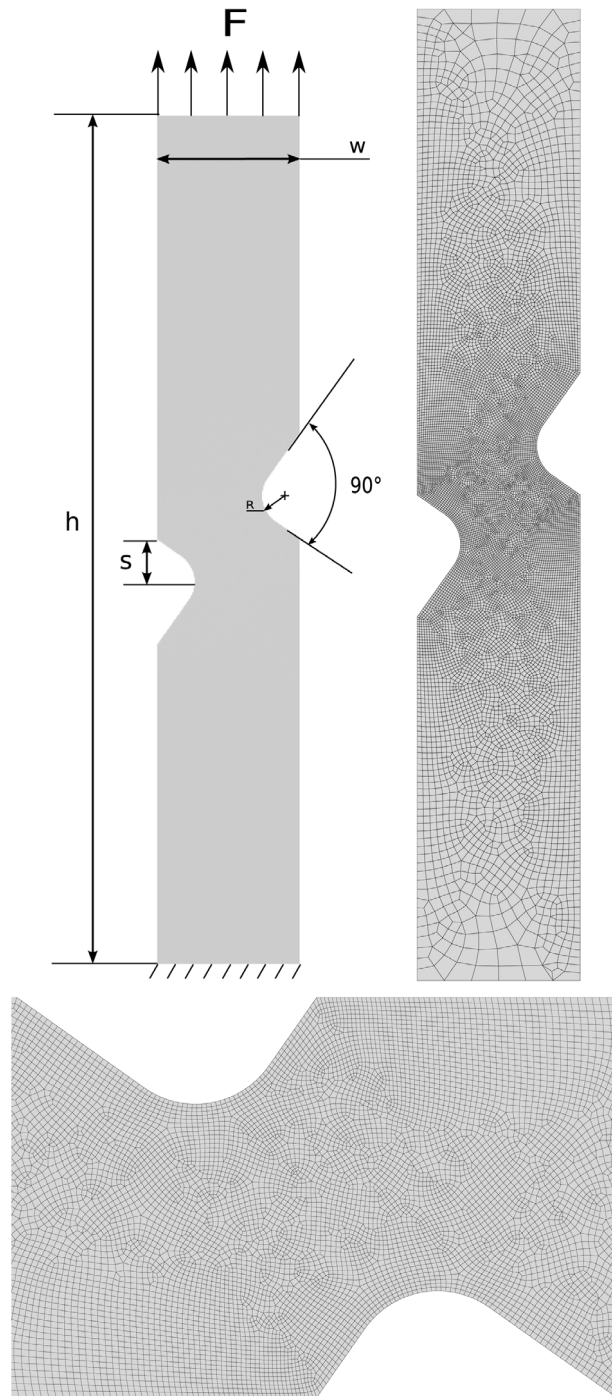*P.A. Sabnis et al. / Comput. Methods Appl. Mech. Engrg. ▮ (▮▮▮▮) ▮▮▮–▮▮▮*   17

Fig. 12. Geometry (top left) and finite element mesh (top right) of the multiaxial creep specimen, close-up view of the mesh in the main deformation zone.

resolution is finer than in Section 3 because the creep sample is significantly smaller than the shear specimen so that the previous model would have been too coarse. The regularisation parameters are therefore selected pragmatically as a compromise between required mesh size and resolution of the fields. The initial opening/cleavage stress was chosen to be $Y_0 = 1000$ MPa. Various combinations of β and H were tested. The simulated creep curves are shown in

ARTICLE IN PRESS

18   *P.A. Sabnis et al. / Comput. Methods Appl. Mech. Engrg. ▮ (▮▮▮▮) ▮▮▮–▮▮▮*
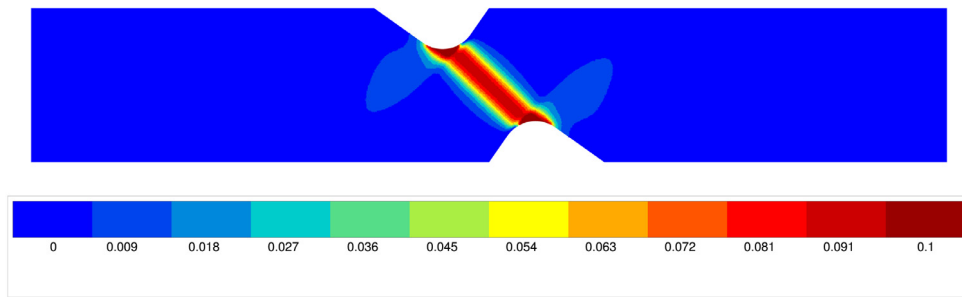
Fig. 13. Accumulated plastic slip field predicted by finite element analysis after 27 h creep.

Fig. 14(b). The 2D simulations promote highly localised damage and rapid cracking, as seen from the brutal tertiary stage in Fig. 14(b). Plane strain conditions are known to promote shear localisation [1].

More realistic creep curves are obtained from 3D computations. The 3D mesh was generated by extruding the 2D fine mesh from the previous section. The 3D model consists of 10 layers of elements along the thickness. 3D simulations using the same material parameters as the ones used for the 2D tests in the previous section led to the results shown in Fig. 14(c) where reasonable agreement is obtained compared to the experiment. The found parameters H and β are given in Table 4. The development of the damage zone is shown in Fig. 15.

The 2D and 3D computations provide the location of crack initiation, the first crack path and a tendency of the crack to branch and bifurcate. The initiated crack is perpendicular to the free surface and must then bifurcate towards the opposite notch zone, as shown in Fig. 16.

The results of the simulated crack propagation can be compared to the crack paths observed in the experiment. The experimental specimen shows an initial crack propagation at an angle of approximately 70° from the loading axis. Following the propagation of this initial crack, a sharp bifurcation is observed towards the opposite notch. Once the abrupt crack deviation has occurred, the crack propagates at an angle of about 30° with respect to the loading axis, see Fig. 16(a). These observations are in good agreement with the predicted crack paths as shown in Fig. 16(b) where the crack path predicted in one 2D computation is directly compared to the experimental one. Note that the damage field is shown in Fig. 16(b) with respect to the undeformed configuration, in contrast to the experimental one. More quantitative comparison is not possible since the creep fracture involves large strains and lattice rotations that are not included in the computational analysis. Significant lattice rotation was observed experimentally in the damage zone of the creep specimen so that the full crack path of Figs. 13 and 15 and crack propagation rate will be modified when considering large deformations. This is left for future work implementing the finite deformation theory.

5. Conclusions

Two–dimensional and three-dimensional finite element simulations of regularised crack initiation and propagation in single crystals under complex loading conditions have been presented for the first time in the literature. They rely on the formulation of a thermodynamically consistent micromorphic coupled crystal plasticity–damage model initially developed for applications in fatigue and used here for shear dominated loading conditions. The model is suited for metal single crystals in which damage localises rapidly into a crack after some plastic deformation in the absence of diffuse damage zone, as it is the case in single crystal nickel-based superalloys. It takes full account of elastic, plastic and damage anisotropy, the latter being introduced via the consideration of damage along {111} planes in FCC crystals. The regularisation relies on one single micromorphic variable representing accumulated damage with respect to all four {111} planes, which represents a limited computational cost. The proposed coupling between plasticity and damage goes through a quadratic free energy potential function of two internal variables of accumulated viscoplastic slip and damage. It was shown that low values of the softening modulus H promote plasticity driven fracture modes, i.e. crack growing through plastically highly deformed zones, whereas large values lead to more brittle responses in the sense that the positive normal stress becomes the limiting factor.

The model predicts a realistic crack path in a four-point single crystal specimen with dominant shear loading. Under creep loading conditions, the crack initiation location, the subsequent short propagation followed by crack bifurcation into the final crack were accurately predicted by the model in agreement with recent experiments on single crystal

ARTICLE IN PRESS

P.A. Sabnis et al. / Comput. Methods Appl. Mech. Engrg. ∎ *(∎∎∎∎)* ∎∎∎–∎∎∎　　　　19
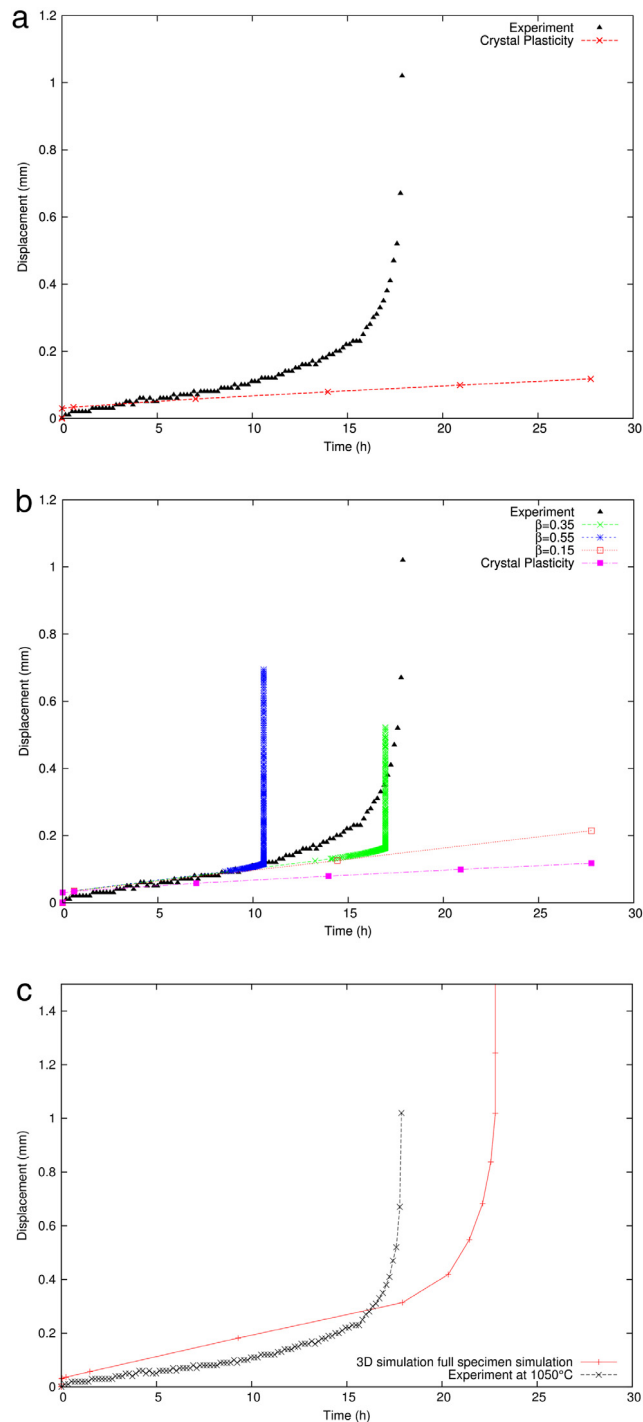
Fig. 14. Overall creep curves for (a) crystal plasticity without damage, (b) two-dimensional and (c) three-dimensional microdamage simulations.

nickel-based superalloys at high temperature. The provided simulations show that regularised anisotropic continuum damage mechanics is amenable to three-dimensional finite element simulations of realistic components as encountered in jet engines.

This work opens many prospects in the simulation of crack initiation and propagation in crystalline solids. The implementation of the finite deformation version of the model, as proposed in [21], represents the next step for
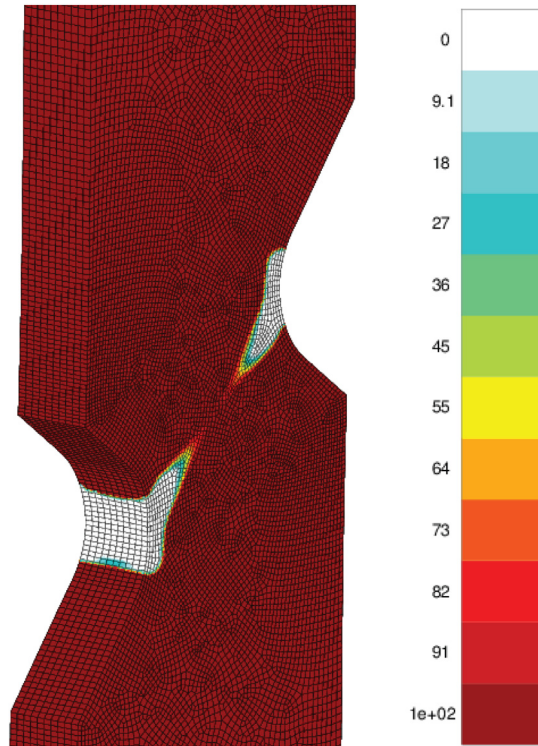
ARTICLE IN PRESS

20 *P.A. Sabnis et al. / Comput. Methods Appl. Mech. Engrg. ▮ (▮▮▮▮) ▮▮▮–▮▮▮*

Fig. 15. Crack growth in a 3D creep simulation: field of the damage threshold variable Y after 18 h creep, see Fig. 14.
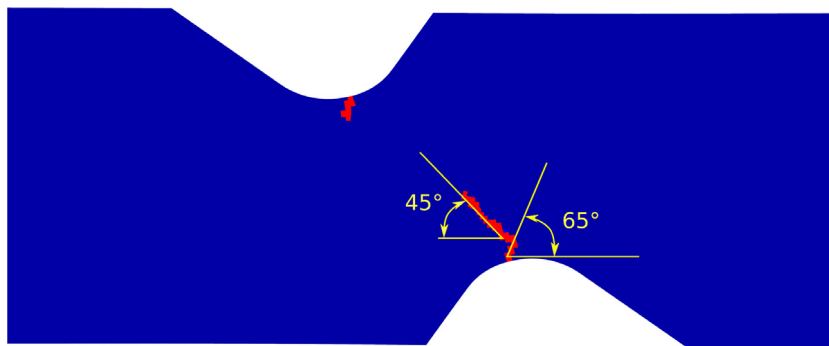
Table 3
Slip system and Damage system definitions used in fracture simulations presented in the previous sections.

System No.	System type	Plane normals			In-plane directions		
		n_1	n_2	n_3	l_1	l_2	l_3
1	Octahedral Slip	1	1	1	$\bar{1}$	0	1
2	Octahedral Slip	1	1	1	0	$\bar{1}$	1
3	Octahedral Slip	1	1	1	$\bar{1}$	1	0
4	Octahedral Slip	1	$\bar{1}$	1	$\bar{1}$	0	1
5	Octahedral Slip	1	$\bar{1}$	1	0	1	1
6	Octahedral Slip	1	$\bar{1}$	1	1	1	0
7	Octahedral Slip	$\bar{1}$	1	1	0	$\bar{1}$	1
8	Octahedral Slip	$\bar{1}$	1	1	1	1	0
9	Octahedral Slip	$\bar{1}$	1	1	1	0	1
10	Octahedral Slip	1	1	$\bar{1}$	$\bar{1}$	1	0
11	Octahedral Slip	1	1	$\bar{1}$	1	0	1
12	Octahedral Slip	1	1	$\bar{1}$	0	1	1
1	Damage	1	1	1	–	–	–
2	Damage	1	1	$\bar{1}$	–	–	–
3	Damage	$\bar{1}$	1	1	–	–	–
4	Damage	1	$\bar{1}$	1	–	–	–

that purpose. The second step deals with the use of more realistic constitutive equations for the crystal plasticity model. The constitutive equations used in the present work involve simple linear hardening or softening moduli which are not sufficient for a quantitative comparison with experiments. This is due to the fact that a consistent thermodynamic framework was preferred in order to ensure the regularisation properties of the model and that more elaborate existing constitutive equations are not necessarily easily derivable from two potential functions. The constitutive equations should be improved especially regarding the creep behaviour that is influenced by softening

ARTICLE IN PRESS

P.A. Sabnis et al. / Comput. Methods Appl. Mech. Engrg. ▮ (▮▮▮▮) ▮▮▮–▮▮▮ 21
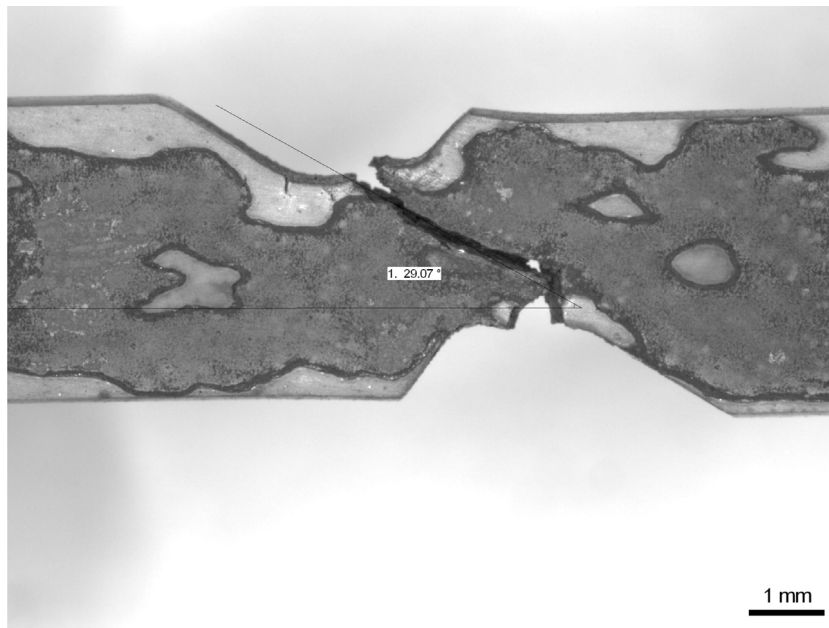
(a) Experimental crack growth observation.

(b) Crack growth predicted by the microdamage model.

Fig. 16. Comparison of crack paths in the experiment and according to the simulation for the creep test.

Table 4
Material parameters for single crystal nickel-based superalloys AM1 at 950 °C and MC2 at 1050 °C.

Material	Fig. no.	C11 (MPa)	C44 (MPa)	C12 (MPa)	R_0 (MPa)	K (MPa s$^{1/n}$)	n	h (MPa)	Y_0 (MPa)	K_d (MPa.s$^{1/n_d}$)	n_d	H (MPa)	H_χ (MPa)	β
AM1	9(c)	261000.0	93000.0	198000.0	69.0	517.0	5.0	1000.0	1500.0	20.0	2.0	−15000.0	100000.0	0.35
AM1	9(b)	261000.0	93000.0	198000.0	69.0	517.0	5.0	100.0	1500.0	10.0	2.0	−35000.0	100000.0	0.35
AM1	9(a)	261000.0	93000.0	198000.0	69.0	517.0	5.0	100.0	1500.0	10.0	2.0	−45000.0	100000.0	0.35
MC2	16	170042.0	111745.0	97418.0	3.0	900	6.3	9.0	1000.0	20.0	2.0	−12000.0	50000.0	0.55

effects due to microstructure evolution in single crystal nickel-based superalloys, such as coarsening or the so-called γ' rafting [40,64]. The present model is not really suited for ductile tearing of single crystals involving cavity growth and coalescence. Alternative Gurson-type models have been recently extended to single crystals for that purpose, see [65–68].

ARTICLE IN PRESS

22 *P.A. Sabnis et al. / Comput. Methods Appl. Mech. Engrg. ▮ (▮▮▮▮) ▮▮▮–▮▮▮*

Acknowledgements

Appendix. Crystal plasticity material parameters used in the simulations

The material parameters used in the simulation of experimental specimens are listed here. They represent the constitutive behaviour of single crystal nickel-based superalloys AM1 and MC2. It is noted that all the simulations include only octahedral slip systems. Neither cubic slip nor kinematic hardening was accounted for the sake of simplicity and in contrast to the original material model for AM1 [46,69]. The parameter values are given in Table 4. Table 3 provides the list of slip systems and cleavage planes used in the simulations.

References

[1] J. Besson, G. Cailletaud, J.L. Chaboche, S. Forest, Non-linear Mechanics of Materials, Springer, 2010.

[2] J. Lemaitre, R. Desmorat, Engineering Damage Mechanics: Ductile, Creep, Fatigue and Brittle Failures, Springer Verlag, Berlin, 2004.

[3] N. Challamel, D. Halm, A. Dragon, On the non-conservativeness of a class of anisotropic damage models with unilateral effects, C. R. Mecanique 334 (2006) 414–418.

[4] W. Qi, A. Bertram, Anisotropic continuum damage modeling for single crystals at high temperatures, Int. J. Plast. 15 (1999) 1197–1215.

[5] M. Ekh, R. Lillbacka, K. Runesson, A model framework for anisotropic damage coupled to crystal (visco)plasticity, Int. J. Plast. 20 (2004) 2143–2159.

[6] J.L. Bouvard, J.L. Chaboche, F. Feyel, F. Gallerneau, A cohesive zone model for fatigue and creep–fatigue crack growth in single crystal superalloys, Int. J. Fatigue 31 (2009) 868–879.

[7] A. Pandolfi, K. Weinberg, A numerical approach to the analysis of failure modes in anisotropic plates, Eng. Fract. Mech. 78 (2011) 2052–2069.

[8] S. Flouriot, S. Forest, G. Cailletaud, A. Koster, L. Rémy, B. Burgardt, V. Gros, S. Mosset, J. Delautre, Strain localization at the crack tip in single crystal CT specimens under monotonous loading: 3D Finite Element analyses and application to Nickel-base superalloys, Int. J. Fract. 124 (2003) 43–77.

[9] B. Larrouy, P. Villechaise, J. Cormier, O. Berteaux, Grain boundary–slip bands interactions: Impact on the fatigue crack initiation in a polycrystalline forged Ni-based superalloy, Acta Mater. 99 (2015) 325–336.

[10] S. Patil, R. Narasimhan, R. Mishra, Observation of kink shear bands in an aluminium single crystal fracture specimen, Scr. Mater. 61 (2009) 465–468.

[11] R. Narasimhan, H. Subramanya, S. Patil, P. Tandaiya, U. Ramamurty, Stationary crack tip fields in elastic–plastic solids: an overview of recent numerical simulations, J. Phys. D: Appl. Phys. 42 (2009) 214005.

[12] P.A. Sabnis, M. Mazière, S. Forest, N.K. Arakere, F. Ebrahimi, Effect of secondary orientation on notch-tip plasticity in superalloy single crystals, Int. J. Plast. 28 (2012) 102–123.

[13] P.A. Sabnis, S. Forest, N.K. Arakere, V.A. Yastrebov, Crystal plasticity analysis of cylindrical indentation on a Ni-base single crystal superalloy, Int. J. Plast. 51 (2013) 200–217.

[14] J.D. Hochhalter, D.J. Littlewood, R.J. Christ Jr., M.G. Veilleux, J.E. Bozek, A.R. Ingraffea, A.M. Maniatty, A geometric approach to modeling microstructurally small fatigue crack formation: II. Physically based modeling of microstructure-dependent slip localization and actuation of the crack nucleation mechanism in AA 7075–T651, Modelling Simul. Mater. Sci. Eng. 18 (2010) 045004.

[15] K.I. Elkhodary, M.A. Zikry, A fracture criterion for finitely deforming crystalline solids—The dynamic fracture of single crystals, J. Mech. Phys. Solids 59 (2011) 2007–2022.

[16] J. Li, H. Proudhon, A. Roos, V. Chiaruttini, S. Forest, Crystal plasticity finite element simulation of crack growth in single crystals, Comput. Mater. Sci. 90 (2014) 191–197.

[17] H. Proudhon, J. Li, F. Wang, A. Roos, V. Chiaruttini, S. Forest, 3D simulation of short fatigue crack propagation by finite element crystal plasticity and remeshing, Int. J. Fatigue 82 (2016) 238–246.

[18] N. Marchal, S. Flouriot, S. Forest, L. Rémy, Crack–tip stress–strain fields in single crystal nickel–base superalloys at high temperature under cyclic loading, Comput. Mater. Sci. 37 (2006) 42–50.

[19] O. Aslan, S. Forest, Crack growth modelling in single crystals based on higher order continua, Comput. Mater. Sci. 45 (2009) 756–761.

[20] O. Aslan, S. Quilici, S. Forest, Numerical modeling of fatigue crack growth in single crystals based on microdamage theory, Int. J. Damage Mech. 20 (2011) 681–705.

[21] O. Aslan, N.M. Cordero, A. Gaubert, S. Forest, Micromorphic approach to single crystal plasticity and damage, Internat. J. Engrg. Sci. 49 (2011) 1311–1325.

[22] S. Forest, The micromorphic approach for gradient elasticity, viscoplasticity and damage, ASCE J. Eng. Mech. 135 (2009) 117–131.

[23] G. Hütter, U. Mühlich, M. Kuna, Micromorphic homogenization of a porous medium: elastic behavior and quasi-brittle damage, Contin. Mech. Thermodyn. 27 (2015) 1059–1072.

ARTICLE IN PRESS

P.A. Sabnis et al. / Comput. Methods Appl. Mech. Engrg. ▮ (▮▮▮▮) ▮▮▮–▮▮▮

23

[24] C. Miehe, A multifield incremental variational framework for gradient type standard dissipative solids, J. Mech. Phys. Solids 59 (2011) 898–923.

[25] S. Wulfinghoff, T. Böhlke, Equivalent plastic strain gradient enhancement of single crystal plasticity: theory and numerics, Proc. R. Soc. Lond. Ser. A Math. Phys. Eng. Sci. 468 (2012) 2682–2703.

[26] S. Wulfinghoff, E. Bayerschen, T. Böhlke, Conceptual difficulties in plasticity including the gradient of one scalar plastic field variable, PAMM Proc. Appl. Math. Mech. 14 (2014) 317–318.

[27] C. Miehe, F. Welschinger, M. Hofacker, A phase field model of electromechanical fracture, J. Mech. Phys. Solids 58 (2010) 1716–1740.

[28] C. Miehe, F. Welschinger, M. Hofacker, Thermodynamically consistent phase-field models of fracture: Variational principles and multi-field FE implementations, Internat. J. Numer. Methods Engrg. 83 (2010) 1273–1311.

[29] M. Hofacker, C. Miehe, Continuum phase field modeling of dynamic fracture: Variational principles and staggered FE implementation, Int. J. Fract. 178 (2012) 113–129.

[30] M. Hofacker, C. Miehe, A phase field model of dynamic fracture: Robust field updates for the analysis of complex crack patterns, Internat. J. Numer. Methods Engrg. 93 (2013) 276–301.

[31] O. Aslan, S. Forest, The micromorphic versus phase field approach to gradient plasticity and damage with application to cracking in metal single crystals, in: R. de Borst, E. Ramm (Eds.), Multiscale Methods in Computational Mechanics, in: Lecture Notes in Applied and Computational Mechanics, vol. 55, Springer, 2011, pp. 135–154.

[32] J. Vignollet, S. May, R. Borst, C. Verhoosel, Phase–field models for brittle and cohesive fracture, Meccanica 49 (2014) 2587–2601.

[33] A. Abdollahi, I. Arias, Phase-field simulation of anisotropic crack propagation in ferroelectric single crystals: effect of microstructure on the fracture process, Modelling Simul. Mater. Sci. Eng. 19 (2011) 074010.

[34] J.D. Clayton, J. Knap, Nonlinear phase field theory for fracture and twinning with analysis of simple shear, Phil. Mag. 95 (2015) 2661–2696.

[35] C.A.H. Padilla, B. Markert, A coupled ductile fracture phase-field model for crystal plasticity, Contin. Mech. Thermodyn. (2015).

[36] P. Michelis, F. Gallerneau, N. Marchal, S. Forest, L. Rémy, SOCRAX—Expanding The Limits of Single Crystal Superalloys Through Short Crack Fracture Mechanics Analysis. Deliverable No. D2.4.2 - Report - The Characterisation of The Short/long Crack Growth Behaviour of The Single Crystal Superalloys AM1 and PWA1487, Technical Report, ONERA, France, 2002.

[37] V. Spitas, C. Spitas, P. Michelis, Real-time measurement of shear fatigue crack propagation at high-temperature using the potential drop technique, Measurement 41 (2008) 424–432.

[38] V. Spitas, C. Spitas, P. Michelis, A three-point electrical potential difference method for in situ monitoring of propagating mixed-mode cracks at high temperature, Measurement 43 (2010) 950–959.

[39] J.B. le Graverend, J. Cormier, S. Kruch, F. Gallerneau, J. Mendez, Microstructural parameters controlling high-temperature creep life of the nickel-base single-crystal superalloy MC2, Metall. Mater. Trans. A 43A (2012) 3988–3997.

[40] J.B. le Graverend, J. Cormier, M. Jouiad, F. Gallerneau, P. Paulmier, F. Hamon, Effect of γ' precipitation on non–isothermal creep and creep–fatigue behaviour of nickel base superalloy MC2, Mater. Sci. Eng. A 527 (2010) 5295–5302.

[41] K. Saanouni, A. Abdul-Latif, Micromechanical Modeling of low cycle fatigue under complex loadings—Part I. Theoretical Formulation, Int. J. Plast. 12 (1996) 1111–1121.

[42] M. Boudifa, K. Saanouni, J.L. Chaboche, A micromechanical model for inelastic ductile damage prediction in polycrystalline metals for metal forming, Int. J. Mech. Sci. 51 (2009) 453–464.

[43] R.H.J. Peerlings, R. de Borst, W.A.M. Brekelmans, J.H.P. Vree, Gradient enhanced damage for quasi-brittle materials, Internat. J. Numer. Methods Engrg. 39 (1996) 3391–3403.

[44] R. Parisot, S. Forest, A. Pineau, F. Grillon, X. Démonet, J.-M. Mataigne, Deformation and damage mechanisms of zinc coatings on galvanized steel sheets, Part I: Deformation modes, Metall. Mater. Trans. 35A (2004) 797–811.

[45] R. Parisot, S. Forest, A. Pineau, F. Nguyen, X. Démonet, J.-M. Mataigne, Deformation and damage mechanisms of zinc coatings on galvanized steel sheets, Part II: Damage modes, Metallurgical and Materials Transactions 35A (2004) 813–823.

[46] L. Méric, P. Poubanne, G. Cailletaud, Single crystal modeling for structural calculations. Part 1: Model presentation, J. Eng. Mater. Technol. 113 (1991) 162–170.

[47] S. Forest, R. Sievert, Elastoviscoplastic constitutive frameworks for generalized continua, Acta Mech. 160 (2003) 71–111.

[48] M.E. Gurtin, Generalized Ginzburg-Landau and Cahn-Hilliard equations based on a microforce balance, Physica D 92 (1996) 178–192.

[49] Z–set package, Non-linear material & structure analysis suite, 2013. www.zset-software.com.

[50] J. Bergheau, J. Leblond, G. Perrin, A new numerical implementation of a second-gradient model for plastic porous solids, with an application to the simulation of ductile rupture tests, Comput. Methods Appl. Mech. Engrg. 268 (2014) 105–125.

[51] R. Bargellini, D. Halm, A. Dragon, Modelling of quasi-brittle behaviour: a discrete approach coupling anisotropic damage growth and frictional sliding, Eur. J. Mech. A Solids 27 (2008) 564–581.

[52] C. Mayr, G. Eggeler, G. Webster, G. Peter, Double shear creep testing of superalloy single crystals at temperatures above 1000°C, Mater. Sci. Eng. A 199 (1995) 121–130.

[53] G. Peter, M. Probst-Hein, K.M.K. Neuking, G. Eggeler, Finite element stress and strain analysis of a double shear creep specimen, Mater.wiss. Werkst.tech 28 (1997) 457–464.

[54] F. Gallerneau, A. Sanson, SOCRAX—Expanding the Limits of Single Crystal Superalloys Through Short Crack Fracture Mechanics Analysis. Deliverable No. D5.1 - Report - Application of the SOCRAX Methods to Aeronautical Components and Tests Cases, Technical Report, ONERA, 2004.

[55] D. Chatterjee, N. Hazari, R. Mitra, Microstructure and creep behavior of DMS4-type nickel based superalloy single crystals with orientations near ⟨001⟩ and ⟨011⟩, Mater. Sci. Eng. A 528 (2010) 604–613.

[56] A. Staroselsky, B.N. Cassenti, Creep, plasticity, and fatigue of single crystal superalloy, Int. J. Solids Struct. 48 (2011) 2060–2075.

[57] Q.M. Yu, Y. Wang, Z.X. Wen, Z.F. Yue, Notch effect and its mechanism during creep rupture of nickel-base single crystal superalloys, Materials Science and Engineering A 520 (2009) 1–10.

ARTICLE IN PRESS

24   *P.A. Sabnis et al. / Comput. Methods Appl. Mech. Engrg. ▮ (▮▮▮▮) ▮▮▮–▮▮▮*

[58] A.C. Yeh, A. Sato, T. Kobayashi, H. Harada, On the creep and phase stability of advanced Ni-base single crystal superalloys, Mater. Sci. Eng. A 490 (2008) 445–451.

[59] T. Tinga, W.A.M. Brekelmans, M.G.D. Geers, Time-incremental creep-fatigue damage rule for single crystal Ni-base superalloys, Mater. Sci. Eng. A 508 (2009) 200–208.

[60] J. Cormier, X. Milhet, J. Mendez, Anisothermal creep behavior at very high temperature of a Ni-based superalloy single crystal, Mater. Sci. Eng. A 483–484 (2008) 594–597.

[61] T. Sugui, Z. Jinghua, Z. Huihua, Y. Hongcai, X. Yongbo, H. Zhuangqi, Aspects of primary creep of a single crystal nickel-base superalloy, Mater. Sci. Eng. A 262 (1999) 271–278.

[62] V. Seetharaman, A.D. Cetel, Thickness debit in creep properties of PWA 1484, in: Superalloys 2004, TMS, 2004.

[63] C. Pragassam, A. Helstroffer, Analyse Des Micro-mécanismes D'endommagement En Fluage, Technical Report, ENSMA, 2011.

[64] A. Gaubert, M. Jouiad, J. Cormier, Y. Le Bouar, J. Ghighi, Three–dimensional imaging and phase–field simulations of the microstructure evolution during creep test of ⟨011⟩–oriented Ni-based superalloys, Acta Mater. 84 (2015) 237–255.

[65] X. Han, J. Besson, S. Forest, B. Tanguy, S. Bugat, A yield function for single crystals containing voids, Int. J. Solids Struct. 50 (2013) 2115–2131.

[66] J. Paux, L. Morin, R. Brenner, D. Kondo, An approximate yield criterion for porous single crystals, European Journal of Mechanics A/solids 51 (2015) 1–10.

[67] A. Mbiakop, A. Constantinescu, K. Danas, On void shape effects of periodic elasto-plastic materials subjected to cyclic loading, European Journal of Mechanics A/Solids 49 (2015) 481–499.

[68] A. Mbiakop, A. Constantinescu, K. Danas, An analytical model for porous single crystals with ellipsoidal voids, J. Mech. Phys. Solids 84 (2015) 436–467.

[69] R. Chieragatti, L. Remy, Influence of orientation on the low cycle fatique of MAR-M200 single crystals ar 650°C II: Cyclic stress–strain behaviour, Mater. Sci. Eng. A 141 (1991) 11–22.